AGU PUBLICATIONS

JGR

Journal of Geophysical Research: Space Physics

RESEARCH ARTICLE
10.1002/2016JA022524

Key Points:
- Comparison of ion Bernstein instabilities driven by ring and shell proton distributions
- Growth rate pattern is determined by the resonant condition and the velocity distribution function
- Shell-driven Bernstein growth rates exhibit more complex pattern due to curved geometry of shell

Correspondence to:
K. Min,
kmin@auburn.edu

Citation:
Min, K., and K. Liu (2016), Understanding the growth rate patterns of ion Bernstein instabilities driven by ring-like proton velocity distributions, *J. Geophys. Res. Space Physics*, *121*, 3036–3049, doi:10.1002/2016JA022524.

Received 9 FEB 2016
Accepted 14 MAR 2016
Accepted article online 18 MAR 2016
Published online 9 APR 2016

Understanding the growth rate patterns of ion Bernstein instabilities driven by ring-like proton velocity distributions

Kyungguk Min[1] and Kaijun Liu[1]

[1]Department of Physics, Auburn University, Auburn, Alabama, USA

Abstract Fast magnetosonic waves in Earth's inner magnetosphere, which have as their source ion Bernstein instabilities, are driven by hot proton velocity distributions (f_p) with $\partial f_p(v_\perp)/\partial v_\perp > 0$. Two typical types of distributions with such features are ring and shell velocity distributions. Both have been used in studies of ion Bernstein instabilities and fast magnetosonic waves, but the differences between instabilities driven by the two types of distributions have not been thoroughly addressed. The present study uses linear kinetic theory to examine and understand these differences. It is found that the growth rate pattern is primarily determined by the cyclotron resonance condition and the structure of the velocity distribution in gyroaveraged velocity space. For ring-driven Bernstein instabilities, as the parallel wave number ($k_\parallel$) increases, the discrete unstable modes approximately follow the corresponding proton cyclotron harmonic frequencies while they become broader in frequency space. At sufficiently large $k_\parallel$, the neighboring discrete modes merge into a continuum. In contrast, for shell-driven Bernstein instabilities, the curved geometry of the shell velocity distribution in gyroaveraged velocity space results in a complex alternating pattern of growth and damping rates in frequency and wave number space and confines the unstable Bernstein modes to relatively small $k_\parallel$. In addition, when $k_\parallel$ increases, the unstable modes are no longer limited to the proton cyclotron harmonic frequencies. The local growth rate peak near an exact harmonic at small $k_\parallel$ bifurcates into two local peaks on both sides of the harmonic when $k_\parallel$ becomes large.

1. Introduction

Enhanced magnetic and electric field fluctuations at frequencies between the proton cyclotron frequency (Ω_p) and the lower hybrid frequency (ω_{lh}) and at propagation nearly perpendicular to the background magnetic field ($\mathbf{B}_0$) are observed frequently near the magnetic equatorial plane of the terrestrial magnetosphere [*Santolík et al.*, 2004; *Němec et al.*, 2005, 2006; *Meredith et al.*, 2008; *Ma et al.*, 2013; *Hrbáčková et al.*, 2015; *Posch et al.*, 2015]. *Russell et al.* [1970] first reported broadband electromagnetic signals confined to an equatorial region within ~ 2° of magnetic latitude, thus initially labeled them as "equatorial noise." Later, *Gurnett* [1976] reported that these signals exhibit a discrete structure in frequency space at harmonics of ion cyclotron frequencies, suggesting that cyclotron resonances with ions rather than bounce resonance with electrons are the likely source of free energy. Since then, there has been increasing observational evidence showing that the dispersion properties of these electromagnetic signals are consistent with those of the low-frequency fast magnetosonic mode in magnetohydrodynamic theory [e.g., *Boardsen et al.*, 1992; *Walker et al.*, 2015]. Hence, these electromagnetic fluctuations are more commonly called "fast magnetosonic waves."

Fast magnetosonic waves tend to occur more frequently on the dayside [*Ma et al.*, 2015]. Particle observations associated with such waves show energetic ring current proton velocity distributions $f_p(\mathbf{v})$ as having a velocity ring feature or, more generally, $\partial f_p(v_\perp)/\partial v_\perp > 0$ [*Meredith et al.*, 2008; *Chen et al.*, 2011; *Xiao et al.*, 2013; *Ma et al.*, 2014; *Zhou et al.*, 2014; *Balikhin et al.*, 2015], where $\perp$ denotes directions perpendicular to $\mathbf{B}_0$. *Chen et al.* [2010a, 2010b] carried out ring current simulations to show that such proton velocity distributions can arise primarily from dusk to dawn as a result of energy-dependent drift of injected ring current ions. Statistical observations suggest that dusk permits more of such proton distributions than does dawn [*Meredith et al.*, 2008; *Thomsen et al.*, 2011], due perhaps to stabilization of the initially unstable distributions by self-generated fast magnetosonic waves, the mechanism missing in the ring current simulations [*Chen et al.*, 2010a, 2010b].

With a sufficient positive slope of $f_p(v_\perp)$, kinetic linear dispersion theory in a homogeneous, collisionless, magnetized plasma predicts unstable proton Bernstein modes at $0 < k_\parallel \ll k_\perp$ and near harmonics of Ω_p [e.g., *Gul'elmi et al.*, 1975; *Perraut et al.*, 1982; *Boardsen et al.*, 1992; *Horne et al.*, 2000], where k denotes the wave number and $\parallel$ denotes the direction parallel to $\mathbf{B}_0$. *Perraut et al.* [1982] considered a two-component proton velocity distribution consisting of a cold proton background and a cold proton ring for linear dispersion analyses. With $k_\parallel = 0$ and a sufficiently tenuous cold proton ring component consistent with plasma conditions found in the inner magnetosphere, they showed that the proton ring-driven instabilities are excited near the crossings between the fast magnetosonic mode and the harmonics of the various Bernstein modes, only if the perpendicular ring speed is larger than the Alfvén speed. With a sufficiently dense cold proton ring component; however, they also showed that the instabilities can be excited substantially away from the fast magnetosonic mode toward decreasing phase speeds.

Numerous studies have since considered thermal ions and electrons [e.g., *Boardsen et al.*, 1992; *McClements et al.*, 1994; *Horne et al.*, 2000; *Denton et al.*, 2010; *Gary et al.*, 2010, 2011]. *Boardsen et al.* [1992] considered a tenuous thermal proton ring by subtracting a cooler bi-Maxwellian from a warmer bi-Maxwellian and showed, using kinetic linear dispersion theory, that the proton cyclotron harmonic instabilities are found within the vicinity of the cold plasma fast magnetosonic mode and the unstable frequency range is affected by the local Alfvén speed. *McClements et al.* [1994] used a more general proton ring

$$
\begin{aligned}
f_r &= \frac{n_r}{\pi^{3/2}\theta_{\parallel r}\theta_{\perp r}^2 C_r} e^{-v_\parallel^2/\theta_{\parallel r}^2} e^{-(v_\perp - v_r)^2/\theta_{\perp r}^2}, \\
C_r &= e^{-v_r^2/\theta_{\perp r}^2} + \sqrt{\pi}\left(\frac{v_r}{\theta_{\perp r}}\right)\mathrm{erfc}\left(-\frac{v_r}{\theta_{\perp r}}\right),
\end{aligned}
\tag{1}
$$

where n_r and v_r denote the ring density and the ring speed, respectively, $\theta_{\parallel r}$ and $\theta_{\perp r}$ denote the ring thermal speeds parallel and perpendicular to $\mathbf{B}_0$, respectively, and $\mathrm{erfc}(x)$ is the complementary error function. They showed that thermal effects allow the proton cyclotron harmonic instabilities to grow at wave normal angles out to at least 10° from the directions strictly perpendicular to $\mathbf{B}_0$. Later, *Min and Liu* [2016] carried out linear dispersion analyses and particle-in-cell simulations using the proton ring distributions of equation (1) to show that not only the proton Bernstein modes but also the Alfvén-cyclotron mode can simultaneously develop. For the proton ring velocity distributions considered, although the maximum linear theory growth rate of the Alfvén-cyclotron instability was always smaller than that of the fastest growing Bernstein mode, the particle-in-cell simulations consistently yielded larger saturation amplitudes for the Alfvén-cyclotron instability.

Gary et al. [2010] considered a dense thermal proton shell (relevant to the situation in the plasma sheet boundary layer) by subtracting a cooler Maxwellian from a warmer Maxwellian and showed the decreasing phase speed of the fundamental mode with decreasing beta. *Liu et al.* [2011] and *Min and Liu* [2015a] extended their linear analyses to a more general proton shell (equation (2) below with $\sigma_s = 0$), and *Min and Liu* [2015b] showed that the instability transition between the Bernstein-like and magnetosonic-like regimes is more strongly affected by the shell density than the shell speed while other parameters are fixed. *Min et al.* [2016] carried out linear dispersion analyses and particle-in-cell simulations for the partial shell velocity distribution

$$
\begin{aligned}
f_s &= \frac{n_s}{\pi^{3/2}\theta_s^3 C_s} e^{-(v - v_s)^2/\theta_s^2} \sin^{\sigma_s}\alpha, \\
C_s &= \left[\frac{v_s}{\theta_s} e^{-v_s^2/\theta_s^2} + \sqrt{\pi}\left(\frac{1}{2} + \frac{v_s^2}{\theta_s^2}\right)\mathrm{erfc}\left(-\frac{v_s}{\theta_s}\right)\right]\frac{\Gamma(1 + \sigma_s/2)}{\Gamma(1.5 + \sigma_s/2)},
\end{aligned}
\tag{2}
$$

where α is the pitch angle, $v \equiv \sqrt{v_\perp^2 + v_\parallel^2}$, n_s, v_s, and θ_s are the shell density, the shell speed and the shell thermal speed, respectively, and $\Gamma(x)$ is the Euler gamma function. They investigated the critical σ_s value at which the Alfvén-cyclotron mode and the proton Bernstein modes saturate at the same level and suggested that since observed fast magnetosonic waves are often not accompanied by electromagnetic ion cyclotron waves, the ring-like proton distributions responsible for the excitation of these fast magnetosonic waves should have small anisotropies and be nearly isotropic.

The ring and shell distributions are two typical types of velocity distributions with $\partial f_p(v_\perp)/\partial v_\perp > 0$. They have both been used in the studies of ion Bernstein instabilities and fast magnetosonic waves, but the differences between the instabilities driven by the two types of distributions have not been thoroughly addressed.

In recent studies of these instabilities using proton velocity distributions described by equations (1) and (2) [*Min and Liu*, 2015a, 2016; *Min et al.*, 2016], substantial differences in the growth rate patterns have been noticed—the instabilities are more discrete, more complex, and more closely confined to quasi-perpendicular propagation for a shell [see *Min and Liu*, 2015a, Figure 7] than for a ring [see *Min and Liu*, 2016, Figure 1]. Here these differences are more thoroughly examined using linear kinetic theory. It should be noted that the present study focuses on the proton Bernstein instabilities only, although the Alfvén-cyclotron mode can also be unstable for the ring and partial shell velocity distributions [*Min and Liu*, 2016; *Min et al.*, 2016].

There have been several studies discussing how the proton Bernstein instabilities are related to the ring speed relative to the Alfvén speed for the conditions found in the inner magnetosphere. *Boardsen et al.* [1992] showed that the ring speed should be close to the Alfvén speed to excite fast magnetosonic waves. *Horne et al.* [2000] provided further insights into the relationship between the ring speed and the frequency range where the maximum growth rate should occur. They suggested that growth is possible for the frequencies $> 30\Omega_p$ when the ring speed exceeds the Alfvén speed and for the frequencies $< 30\Omega_p$ when the ring speed exceeds twice the Alfvén speed. *Chen et al.* [2010b] provided more quantitative explanation of this relationship by invoking approximate linear theory. The methodology for the analyses performed in the current paper follows along similar lines to that used by *Chen et al.* [2010b] but consider propagation directions sufficiently away from the strict perpendicular direction.

The paper is organized as follows: section 2 describes an overview of the differences in the proton Bernstein instabilities driven by the ring and the shell distributions using full linear dispersion theory, section 3 derives the approximate growth rate formula, and section 4 uses this formula to explain the differences in the growth rate pattern. Section 5 summarizes the results. We denote the jth species plasma frequency as $\omega_{pj} \equiv \sqrt{4\pi n_j e^2/m_j}$, the jth species cyclotron frequency as $\Omega_j \equiv e_j B_0/m_j c$ (with sign retained), and the jth component beta as $\beta_j \equiv 8\pi n_j T_j/B_0^2$. Additionally, we define $\tilde{\beta}_j \equiv 8\pi n_0 T_j/B_0^2$ following *Gary et al.* [2010]. The Alfvén speed is $v_A \equiv B_0/\sqrt{4\pi n_0 m_p}$, the proton inertial length is $\lambda_p \equiv \sqrt{m_p c^2/4\pi n_0 e^2}$, and the lower hybrid frequency is $\omega_{\mathrm{lh}} = \omega_{pp}/\sqrt{1+\omega_{pe}^2/\Omega_e^2}$. Here n_0 is equal to the unperturbed electron density n_e. We assume $\mathbf{B}_0 = B_0\hat{\mathbf{z}}$, real wave number $\mathbf{k} = k_\perp\hat{\mathbf{x}} + k_\parallel\hat{\mathbf{z}}$ (with $\hat{\mathbf{x}} = \hat{\mathbf{y}} \times \hat{\mathbf{z}}$) and complex wave frequency $\omega = \omega_r + i\gamma$ with $\gamma > 0$ indicating a growing mode.

2. Overview

We consider three different model distribution functions. The first model distribution consists of the relatively dense, relatively cold core Maxwellian proton component f_c and the relatively tenuous, warm ring proton component f_r following equation (1) and will be labeled as "ring model." For the second model, the ring component is replaced with the isotropic shell f_s given by equation (2) with $\sigma_s = 0$. Hence, this model will be labeled as "shell model." For the third model, the ring component is replaced with the partial shell f_s of equation (2) with $\sigma_s = 2$, and this model will be labeled as "partial shell model." For consistency as well as convenience, we adopt base parameters similar to *Min and Liu* [2016] and *Min et al.* [2016] who used the same two-component proton distributions. That is, we choose $\tilde{\beta}_c = 0.002$ and $\theta_{\parallel r}^2/v_A^2 = \theta_{\perp r}^2/v_A^2 = \theta_s^2/v_A^2 = 0.2$. We, however, use more tenuous energetic proton populations with $n_r/n_0 = n_s/n_0 = 0.01$. This is because the approximate growth rate formula, which is derived in section 3 following the approximate linear theory approach [*Kennel*, 1966; *Chen et al.*, 2010b] and used to interpret the growth rate patterns in section 4, relies on the cold plasma dispersion relation and, therefore, favors more tenuous energetic proton populations. For all three cases, electrons are represented by a single Maxwellian distribution with $\beta_e = \tilde{\beta}_c$.

We also adopt a reduced proton-to-electron mass ratio of $m_p/m_e = 100$ and a relatively small light-to-Alfvén speed ratio of $c/v_A = 15$ (equivalent to $\omega_{pe}/\Omega_e = 1.5$), which result in $\omega_{\mathrm{lh}}/\Omega_p \approx 8.3$. This reduces the number of unstable modes involved and simplifies the linear analyses. Our preliminary analyses show that although the absolute magnitude of growth rates will change when the realistic m_p/m_e and a larger c/v_A are used, the overall growth rate patterns which are the main focus of the present paper remain consistent. More thorough analyses of the dependence of the Bernstein instabilities on m_p/m_e are currently underway and will be reported as a separate paper.

Using these parameters and proton model distributions, a full kinetic linear dispersion relation solver [*Min and Liu*, 2015a] is used to calculate the proton Bernstein instabilities driven by the three model distributions and the results are shown in Figures 1a–1c. Additionally, the shapes of the energetic proton components

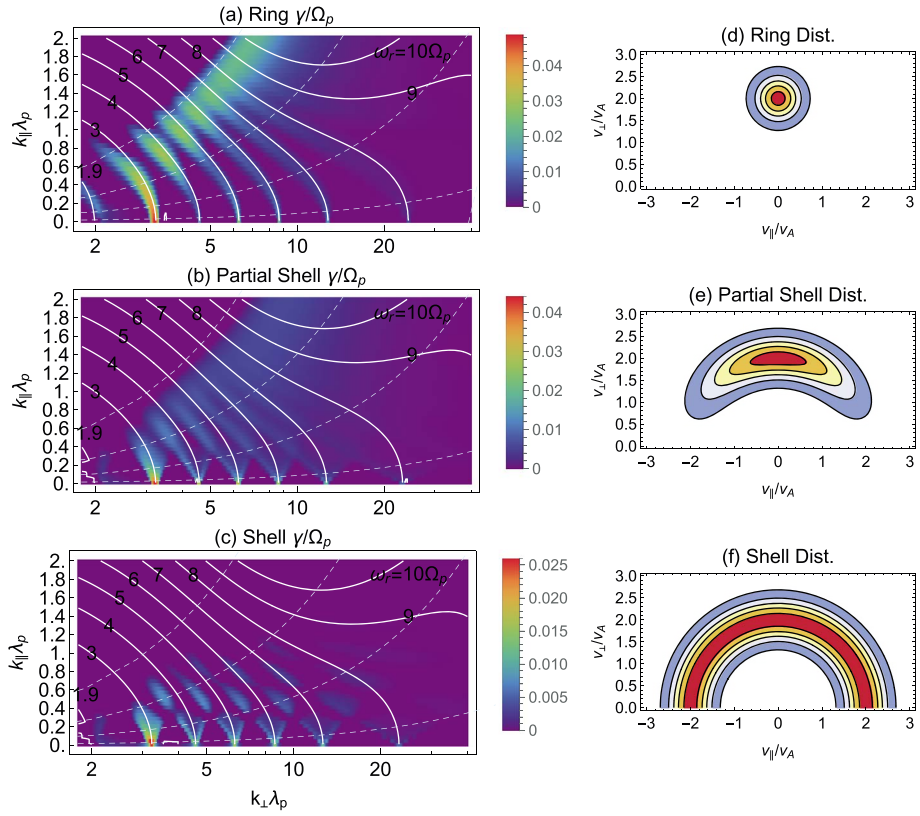

Figure 1. (a–c) Full linear dispersion theory solutions for (Figure 1a) the ring, (Figure 1b) partial shell, and (Figure 1c) shell models. Color intensity (different scales for different plots) and solid contours represent the positive growth rates and real frequencies, respectively. The four dashed curves from Figure 1a denote constant wave normal angle contours at $\psi = 72°, 82°, 87°$ and 89.5°, respectively. (d–f) Contours of the energetic ring-like velocity distribution functions corresponding to the linear results in Figures 1a–1c. The lowest levels delineate 10% of the maximum magnitude of the ring-like velocity distribution functions and the neighboring levels differ by 20%.

that drive the corresponding instabilities are shown to the next in Figures 1d–1f. (The reader is referred to *Min et al.* [2016] for details of handling the partial shell distribution of equation (2) in the linear analyses). The real frequencies represented by the contours are very consistent among all model distributions, whereas the growth rates exhibit significant differences, especially between the ring and shell models—for the parameters chosen and compared to the ring model, the shell model results in a more complex growth rate pattern and the unstable Bernstein modes are confined to much smaller $k_\parallel$. Consistent with the fact that the partial shell model represents a transition from the ring model to the shell model, the growth rate pattern from the partial shell model is apparently in between that of the other two models.

3. Approximate Linear Growth Rate Formula

To investigate the differences shown in Figures 1a–1c more quantitatively, we follow the approximate linear theory approach [*Kennel*, 1966; *Chen et al.*, 2010b]. *Dendy and McClements* [1993] used the extraordinary mode dispersion relation under the assumption that the fluctuating electric fields are polarized in the plane perpendicular to $\mathbf{B}_0$. This is usually a legitimate assumption for the fast magnetosonic waves at quasi-perpendicular propagation. The dispersion relation in this limit [*Dendy and McClements*, 1993] reads

$$0 = D(\omega, \mathbf{k}) \equiv \left(\epsilon_{xx} - k_\parallel^2 \frac{c^2}{\omega^2}\right)\left(\epsilon_{yy} - k^2 \frac{c^2}{\omega^2}\right) + \epsilon_{xy}^2, \tag{3}$$

where the dielectric components, ϵ_{xx}, ϵ_{yy}, and ϵ_{xy} [e.g., *Umeda et al.*, 2012] are

$$\epsilon_{xx} = 1 + 2\pi \sum_N \frac{\omega_{pN}^2}{\omega^2} \sum_{j=-\infty}^{\infty} \frac{j^2 \Omega_N^2}{k_\perp^2} \int_0^\infty \mathrm{d}v_\perp J_j^2 \int_{-\infty}^\infty \frac{k_\parallel \mathrm{d}v_\parallel}{\omega - k_\parallel v_\parallel - j\Omega_N} F_N, \tag{4}$$

$$\epsilon_{yy} = 1 + 2\pi \sum_N \frac{\omega_{pN}^2}{\omega^2} \sum_{j=-\infty}^{\infty} \int_0^{\infty} dv_\perp v_\perp^2 (J_j')^2 \int_{-\infty}^{\infty} \frac{k_\parallel dv_\parallel}{\omega - k_\parallel v_\parallel - j\Omega_N} F_N, \tag{5}$$

and

$$\epsilon_{xy} = 2\pi i \sum_N \frac{\omega_{pN}^2}{\omega^2} \sum_{j=-\infty}^{\infty} \frac{j\Omega_N}{k_\perp} \int_0^{\infty} dv_\perp v_\perp J_j J_j' \int_{-\infty}^{\infty} \frac{k_\parallel dv_\parallel}{\omega - k_\parallel v_\parallel - j\Omega_N} F_N. \tag{6}$$

Here $J_j(k_\perp v_\perp/\Omega_N)$ is the Bessel function of the first kind, $J_j'(x) = dJ_j(x)/dx$, N denotes the Nth plasma component and

$$F_N \equiv \frac{\omega - k_\parallel v_\parallel}{k_\parallel} \frac{\partial f_N}{\partial v_\perp} + v_\perp \frac{\partial f_N}{\partial v_\parallel} = \frac{\omega}{k_\parallel} \frac{\partial f_N}{\partial v_\perp} - \frac{\partial f_N}{\partial \alpha}. \tag{7}$$

In general, equation (3) should be solved numerically for, e.g., complex frequency ω.

To simplify the formulation, we take the approximate linear theory approach [e.g., *Kennel*, 1966; *Chen et al.*, 2010b, 2013] where the real frequency ω_r is determined by the cold plasma dispersion relation of the core plasma components, while the growth rate γ which is much smaller than ω_r is determined by the tenuous energetic component. That is, assuming $|\gamma| \ll \omega_r$, $n_{r,s} \ll n_c$ and $\beta_{c,e} \ll 1$, the real frequency and the growth rate [*Kennel*, 1966; *Chen et al.*, 2013] are respectively obtained from

$$D^{(0)}(\omega_r, \mathbf{k}) = 0 \text{ and } \gamma = -\left. \frac{\Im D^{(1)}(\omega, \mathbf{k})}{\partial D^{(0)}/\partial \omega} \right|_{\omega=\omega_r}, \tag{8}$$

where $D^{(0)}$ is real and denotes the zero-temperature core plasma components' contribution to D and $D^{(1)}$ is complex and denotes the energetic proton component's contribution. Likewise, the dielectric components can be separated into the two lowest order terms:

$$\epsilon_{xx} = \epsilon_{xx}^{(0)} + \epsilon_{xx}^{(1)},\ \epsilon_{xy} = \epsilon_{xy}^{(0)} + \epsilon_{xy}^{(1)},\ \text{and } \epsilon_{yy} = \epsilon_{yy}^{(0)} + \epsilon_{yy}^{(1)}. \tag{9}$$

By substituting equation (9) into equation (3) and collecting the same order terms, $D^{(0)}$ and $D^{(1)}$ can read

$$D^{(0)} = \left(\epsilon_{xx}^{(0)} - k_\parallel^2 \frac{c^2}{\omega^2}\right)\left(\epsilon_{yy}^{(0)} - k^2 \frac{c^2}{\omega^2}\right) + (\epsilon_{xy}^{(0)})^2, \tag{10}$$

and

$$D^{(1)} = 2\epsilon_{xy}^{(0)}\epsilon_{xy}^{(1)} + \left(\epsilon_{yy}^{(0)} - \frac{k^2c^2}{\omega^2}\right)\epsilon_{xx}^{(1)} + \left(\epsilon_{xx}^{(0)} - \frac{k_\parallel^2 c^2}{\omega^2}\right)\epsilon_{yy}^{(1)}, \tag{11}$$

respectively.

For our assumed model distributions, the lowest order zero-temperature dielectric components can be obtained by following the derivation of the cold plasma dispersion relation [e.g., *Stix*, 1992]:

$$\epsilon_{xx}^{(0)} = \epsilon_{yy}^{(0)} = 1 - \frac{1}{2} \sum_{N=e,c} \frac{\omega_{pN}^2}{\omega^2} \sum_{\pm} \frac{\omega}{\omega \mp \Omega_N} \text{ and } \epsilon_{xy}^{(0)} = \frac{i}{2} \sum_{N=e,c} \frac{\omega_{pN}^2}{\omega^2} \sum_{\pm} \mp \frac{\omega}{\omega \mp \Omega_N}. \tag{12}$$

Using equations (4–6), the first order dielectric components which contribute to γ may read

$$\Im \epsilon_{xx}^{(1)} \approx -2\pi^2 \frac{\omega_{pN}^2}{\omega^2} \sum_{j=-\infty}^{\infty} \frac{j^2\Omega_N^2}{k_\perp^2} \int_0^{\infty} dv_\perp J_j^2 F_N \Big|_{v_\parallel = v_{j,res}}, \tag{13}$$

$$\Im \epsilon_{yy}^{(1)} \approx -2\pi^2 \frac{\omega_{pN}^2}{\omega^2} \sum_{j=-\infty}^{\infty} \int_0^{\infty} dv_\perp v_\perp^2 (J_j')^2 F_N \Big|_{v_\parallel = v_{j,res}}, \tag{14}$$

and

$$\Re\epsilon_{xy}^{(1)} \approx 2\pi^2 \frac{\omega_{pN}^2}{\omega^2} \sum_{j=-\infty}^{\infty} \frac{j\Omega_N}{k_\perp} \int_0^\infty \mathrm{d}v_\perp v_\perp J_j J_j' F_N \Big|_{v_\parallel = v_{j,res}}, \tag{15}$$

where $v_{j,\mathrm{res}} \equiv (\omega - j\Omega_N)/k_\parallel$ is the parallel resonant speed and N denotes the energetic proton component. In deriving these terms, the integrations in the parallel velocity component are carried out on the real axis for the principal values of the integrals [e.g., *Chen et al.*, 2013, equation (4)]. The real parts of $\epsilon_{xx}^{(1)}$ and $\epsilon_{yy}^{(1)}$ and the imaginary part of $\epsilon_{xy}^{(1)}$ which do not contribute to γ will not be considered. By substituting the relevant terms into equation (11), the imaginary part of $D^{(1)}$ which determines γ may be written as

$$\Im D^{(1)} = 2\pi^2 \frac{\omega_{pN}^2}{\omega^2} \sum_{j=-\infty}^{\infty} \int_0^\infty \mathrm{d}v_\perp W_j F_N \Big|_{v_\parallel = v_{j,res}}, \tag{16}$$

where W_j is defined as

$$\begin{aligned} W_j &\equiv \left(\frac{k_\perp^2 c^2}{\omega^2} + B\right) \frac{j^2\Omega_N^2}{k_\perp^2} J_j^2 - 2A\frac{j\Omega_N}{k_\perp} v_\perp J_j J_j' + B v_\perp^2 (J_j')^2 \\ &= \left[\sqrt{\left(\frac{k_\perp^2 c^2}{\omega^2} + B\right)} \frac{j\Omega_N}{k_\perp} J_j - \sqrt{B} v_\perp J_j'\right]^2 + 2\frac{j\Omega_N}{k_\perp} v_\perp \left[\sqrt{\left(\frac{k_\perp^2 c^2}{\omega^2} + B\right) B} - A\right] J_j J_j' \\ &= \left[\sqrt{\left(\frac{k_\perp^2 c^2}{\omega^2} + B\right)} \frac{j\Omega_N}{k_\perp} J_j - \sqrt{B} v_\perp J_j'\right]^2. \end{aligned} \tag{17}$$

Here $A = -\epsilon_{xy}^{(0)}/i$ and $B = k_\parallel^2 c^2/\omega^2 - \epsilon_{xx}^{(0)}$, and the dispersion relation (10) has been used to remove the second term in the second line. As *Boardsen et al.* [1992], *Horne et al.* [2000], and *Chen et al.* [2010b] pointed out, equation (16) can be interpreted as follows. The function F_N determines the role (growth if $F_N(v_\perp) > 0$ and damping if $F_N(v_\perp) < 0$) of the jth cyclotron resonant particles at $v_\perp$, whereas $W_j(v_\perp)$ which is nonnegative acts as a weighting function to the contribution of the jth cyclotron resonant particles at certain $v_\perp$ to γ.

We make three points regarding equation (16). First, further analytical evaluation of the integral involving W_j and our base distribution functions (1) and (2) is difficult (cf. see *Vandas and Hellinger* [2015], for the ring distribution). Consequently, many studies utilizing the similar approach rely on numerical techniques [e.g., *Chen et al.*, 2010a, 2010b]. In the present paper numerical integration using Simpson's rule [*Press et al.*, 1992] is utilized. Second, for the reasons discussed in *Chen* [2015], the approximate linear growth rate derived becomes invalid as $k_\parallel$ approaches zero. In the following analyses, the $k_\parallel$ range of interest is $0.1 \lesssim k_\parallel \lambda_p \lesssim 1$ and, as will be shown in the next paragraph, the approximate growth rate formula derived is generally valid in this range. Third, $k_\perp$ is involved only in W_j. So $k_\perp$ scales the perpendicular velocity at which the weighting function peaks and is relevant primarily in regulating the magnitude of the growth rates.

As a validation of the approximate linear dispersion theory described above, Figure 2 compares the real frequencies and the growth rates obtained for the ring and shell models specified in section 2 with the results from our full linear dispersion relation solver [*Min and Liu*, 2015a] at $k_\parallel \lambda_p = 0.15, 0.5$, and 0.8. The real frequencies in the approximate linear dispersion theory are essentially from the cold plasma dispersion relation so they are the same for the ring and shell models. Since the real frequencies calculated from the full linear dispersion relation solver are also similar for the ring and shell models (see the solid contours in Figures 1a and 1c), we here display the comparison of the two sets of real frequencies for the shell model only. As shown in Figures 2a–2c, the real frequencies from the full linear dispersion relation solver are close to the cold plasma dispersion relation but can have multiple dispersion branches (due to ion kinetic effect), which are indicated by the nearly horizontal portions of the solid lines in Figures 2a and 2b and are part of the general electromagnetic ion Bernstein mode solutions. The cold plasma dispersion relation becomes less accurate with increasing $k_\parallel$ for fixed ω_r and with increasing ω_r for fixed $k_\parallel$. Yet the approximate linear growth rates shown in Figures 2d and 2e are generally consistent with the full linear dispersion relation solutions, especially where the peaks and valleys occur. Consequently, the approximate linear growth rate formula derived above is suitable for understanding the significant differences in the growth rate patterns of the proton Bernstein instabilities driven by the two different types of velocity distributions.

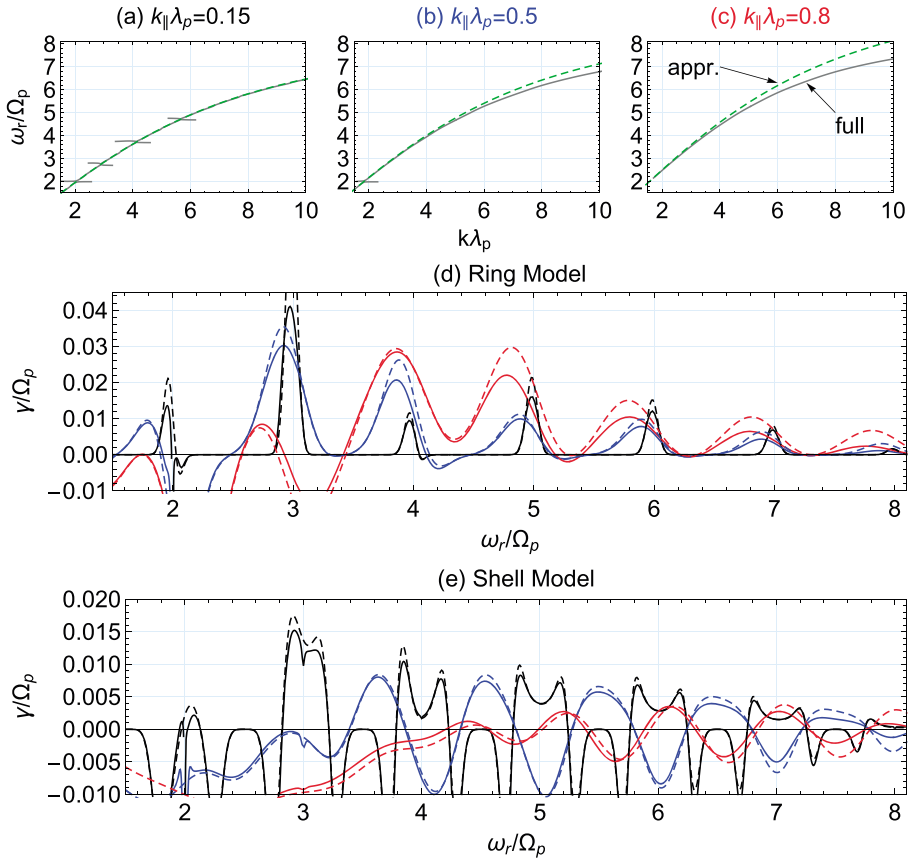

Figure 2. Comparisons of the complex frequencies obtained from full (solid) and approximate (dashed) linear dispersion theory at $k_\parallel\lambda_p = 0.15$ (black), 0.5 (blue) and 0.8 (red). (a–c) Comparison of real frequencies for the shell model. (d) and (e) Comparison of growth rates for the ring and shell models, respectively.

4. Analyses

In this section, we first examine the simpler growth rate pattern driven by the ring model. The noticeable main features are that (1) the discrete unstable modes approximately follow the integer harmonics of Ω_p, (2) they are broadened in frequency space with increasing $k_\parallel$, and that (3) the neighboring modes eventually merge into a continuum at sufficiently large $k_\parallel$ (Figure 1a). We then examine the more complex growth rate pattern driven by the shell model. In contrast to the ring model case, the main features are (1) the split of the local growth rate maxima with increasing $k_\parallel$, (2) the suppression of the instabilities at large $k_\parallel$ ($k_\parallel\lambda_p \gtrsim 1$) and, more interestingly, (3) the alternating pattern of growth and damping in frequency and wave number space (Figures 1c and 2e). The analyses are mainly based on comparing the $\int_0^\infty W_j F_N dv_\perp$, W_j, and F_N terms in equation (16) near the representative harmonic mode and at the relevant cyclotron resonant speeds $v_{j,\mathrm{res}}$ for $k_\parallel\lambda_p = 0.15$, 0.5, and 0.8.

4.1. Ring Model

In this subsection, the growth rate pattern driven by the ring model will be explained. Figure 3a displays $\int_0^\infty W_j F_r dv_\perp$ as a function of frequency near $\omega_r/\Omega_p = 4$ and at $k_\parallel\lambda_p = 0.15$. Here only the $j = 4$ term is shown because $|v_{j,\mathrm{res}}| \gg \theta_{\parallel r}$ for all other js. Note that the shape of the integral is consistent with γ shown in Figure 2d. Figure 3b displays the profile of the parallel component of the ring distribution function of equation (1) and $v_{j,\mathrm{res}}$s at $\omega_r/\Omega_p = 3.92$, 4, and 4.08 for $j = 4$. Since $v_{j,\mathrm{res}}$ is a sensitive function of ω_r due to the smallness of $k_\parallel$, $|v_{j,\mathrm{res}}|$ quickly goes beyond the thermal extent of the ring as ω_r moves away even slightly from $4\Omega_p$. Figure 3c displays W_j (dashed) and F_r (solid) as a function of $v_\perp$ for the three selected ω_r values. Although the peaks of F_r are located near the first valleys of W_j, the overall integral is still positive around $\omega_r = 4\Omega_p$ so the net effect is wave growth. As ω_r moves away from $4\Omega_p$, the magnitude of F_r drops quickly as the corresponding resonant speed for $j = 4$ rapidly goes beyond the thermal extent of the ring protons. This explains why the instabilities

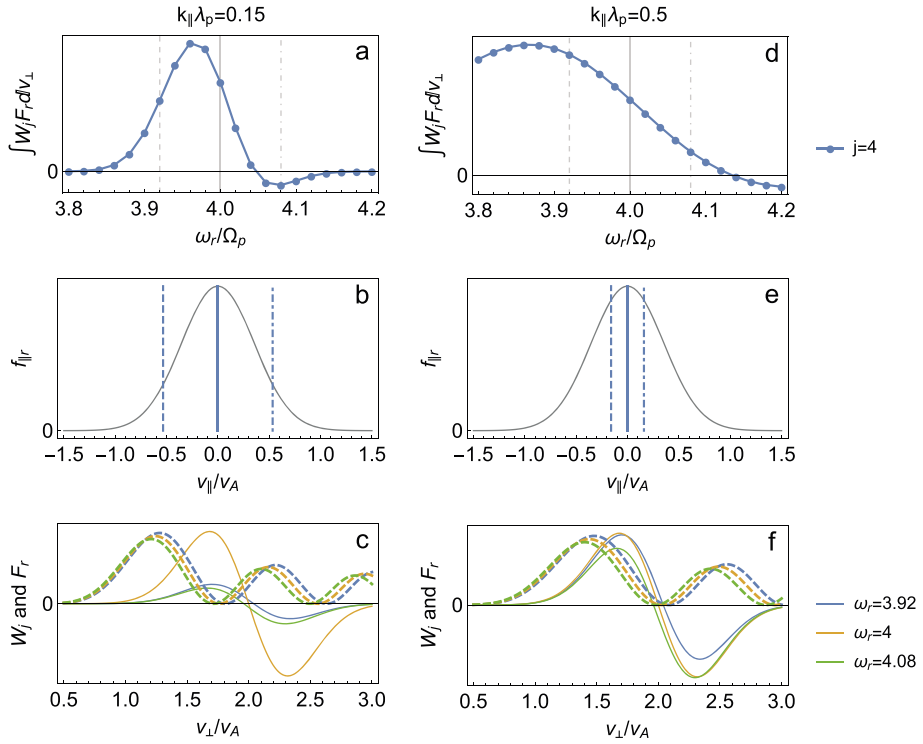

Figure 3. For the ring model, plots of various quantities determining γ at $k_\parallel \lambda_p = 0.15$ (Figures 3a–3c) and 0.5 (Figures 3d–3f). (a and d) Plots of $\int_0^\infty W_j F_s dv_\perp$ as a function of the real frequency. (b and e) Parallel resonant speeds (vertical bars) overlaid on the parallel profile of the ring distribution (solid curves). The corresponding frequencies are denoted with the vertical bars of the same line style on the top plots. (c and f) Plots of W_j (dashed) and F_r (solid) evaluated at the parallel resonant speeds. Note that the two quantities are scaled to fit in one plot.

are confined to discrete frequency ranges around the exact proton cyclotron harmonics at small $k_\parallel$. Another interesting feature is that the peak growth rate is slightly below the exact harmonic frequency of $\omega_r/\Omega_p = 4$ here. This is in fact true at every harmonic (Figure 2d). There are two factors contributing to this. First, the first peak of W_j becomes slightly larger in magnitude and appears at larger $v_\perp$ for $\omega_r < 4\Omega_p$. Second, for our ring model and using $v_\parallel = v_{j,\mathrm{res}}$, F_r can be simplified to

$$F_r = \frac{2f_r \omega_r v_r}{k_\parallel \theta_{\parallel r}^2} \left(j\Omega_p/\omega_r - v_\perp/v_r \right) .$$

So for any fixed $v_\perp$, F_r decreases with increasing ω_r: F_r is larger when $\omega_r/j\Omega_p < 1$ (thus $v_{j,\mathrm{res}} < 0$) than when $\omega_r/j\Omega_p > 1$ (thus $v_{j,\mathrm{res}} > 0$). This indicates that the cyclotron resonant protons contramoving with a wave tend to produce larger γ than the comoving resonant protons.

Figures 3d–3f display the same quantities for $k_\parallel \lambda_p = 0.5$. Compared to the case for $k_\parallel \lambda_p = 0.15$, $v_{j,\mathrm{res}}$ is less sensitive to ω_r due to the increased $k_\parallel$ and as a result, the range of ω_r/Ω_p where $\gamma > 0$ becomes broader. Still, $k_\parallel \lambda_p = 0.5$ is sufficiently small that protons are effectively nonresonant near the half harmonics (where the minimum $|v_{j,\mathrm{res}}|$ is $\sim 2\theta_{\parallel r}$). In addition, one can notice by comparing Figure 3f to 3c that the first peaks of W_j moved to larger $v_\perp$ and became closer to the peaks of F_r. This is because $k_\perp$ decreases with increasing $k_\parallel$ at fixed ω_r/Ω_p (Figure 1a) so the first peak of the Bessel function whose argument is $k_\perp v_\perp/\Omega_p$ appears at larger $v_\perp$. Consequently, $\gamma_{\max}$ near $\omega_r/\Omega_p = 4$ in Figure 2d is significantly larger for $k_\parallel \lambda_p = 0.5$ than for $k_\parallel \lambda_p = 0.15$. Apparently, the opposite situation can happen at other harmonics where $\gamma_{\max}$ is reduced at $k_\parallel \lambda_p = 0.5$ compared to that at $k_\parallel \lambda_p = 0.15$ (Figure 2d). As mentioned in the previous section, $k_\perp$ primarily regulates the magnitude of the growth rates.

Figures 4a–4c display the same quantities for $k_\parallel \lambda_p = 0.8$ and $4 \le \omega_r/\Omega_p \le 5$. In this case, $k_\parallel$ is sufficiently large that $|v_{j,\mathrm{res}}| \sim \theta_{\parallel r}$ at $\omega_r/\Omega_p = 4.5$. As a result, γ can be continuously positive in this frequency range and the originally discrete unstable modes around $\omega_r = 4\Omega_p$ and $5\Omega_p$ at small $k_\parallel$ now start to merge into a

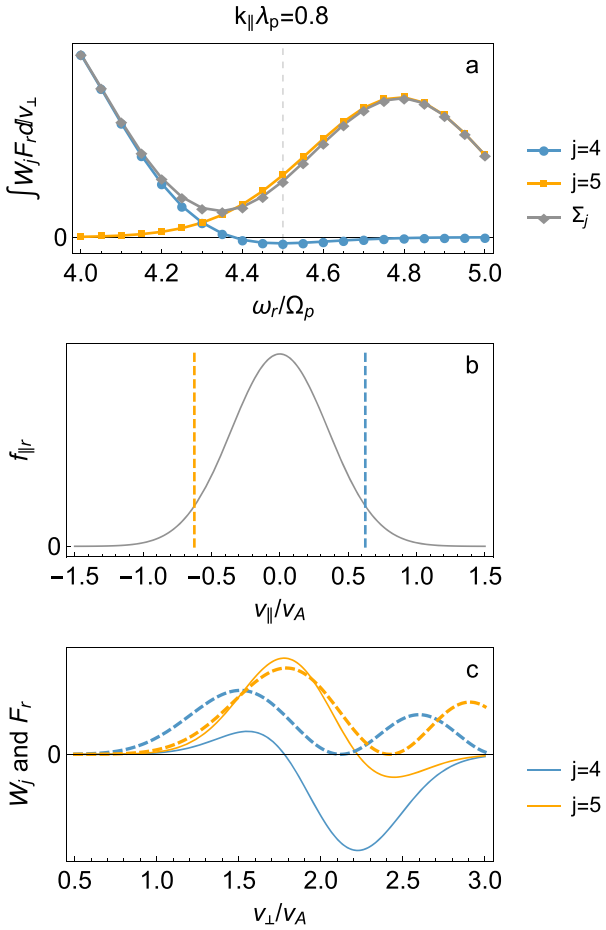

Figure 4. For the case of the ring model and for $k_{\|}\lambda_p = 0.8$. The figure format is the same as Figure 3. The Σ_j label denotes sum of all j contributions.

continuum. As $k_{\|}$ increases further, more j terms come into play so the continuous spectrum of positive γ in frequency space shown in Figure 1a is a result of broadening and merging of the neighboring modes due to more cyclotron harmonic resonances being involved. As a result, $\theta_{\|r}$ is expected to closely affect the minimum $k_{\|}$ at which the neighboring modes start to merge: the larger $\theta_{\|r}$ is, the smaller this minimum $k_{\|}$ would be. It should be noted that the continuous spectrum can also arise when the growth rate is sufficiently large [*Chen et al.*, 2016].

4.2. Shell Model

In this subsection, the same analyses will be applied to the shell model. The shell model is isotropic so F_s in equation (7) is determined solely by the term involving $\partial f_s/\partial v_\perp$ evaluated at $v_{\|} = v_{j,\mathrm{res}}$. Based on the previous analyses, it is expected that this shell model will permit more j terms to be involved due to the wider extent of the shell along the parallel velocity component (see Figures 1d and 1f) and the cyclotron resonant protons near the outskirts of the shell (i.e., at $|v_{\|}| \gtrsim v_s$) will primarily contribute to wave damping due to $\partial f_s/\partial v_\perp < 0$ and hence $F_s < 0$ there.

Figure 5a displays $\int_0^\infty W_j F_s \mathrm{d}v_\perp$ as a function of frequency near $\omega_r/\Omega_p = 4$ and at $k_{\|}\lambda_p = 0.15$. Since $k_{\|}$ is sufficiently small, $|v_{j,\mathrm{res}}|$ is much larger than v_s except for $j = 4$. Therefore, only the $j = 4$ term contributes to γ. The interesting feature here is that the γ profile as a function of the frequency has a local minimum at $\omega_r/\Omega_p \approx 4$ (solid vertical bar). The dashed and dash-dotted vertical bars are located at $\omega_r/\Omega_p = 3.84$ and 4.16 near the two local maxima, respectively. Figure 5b displays the corresponding $v_{j,\mathrm{res}}$ values overlaid with the contours of the shell distribution of equation (2). There apparently exists a range of $v_\perp$ where the values of $\partial f_s/\partial v_\perp$ evaluated at these three vertical bars are positive. Consequently, it is possible to have $\gamma > 0$ at these frequencies. The local minimum at $\omega_r/\Omega_p = 4$ can be explained from Figure 5c that shows as a function of $v_\perp$

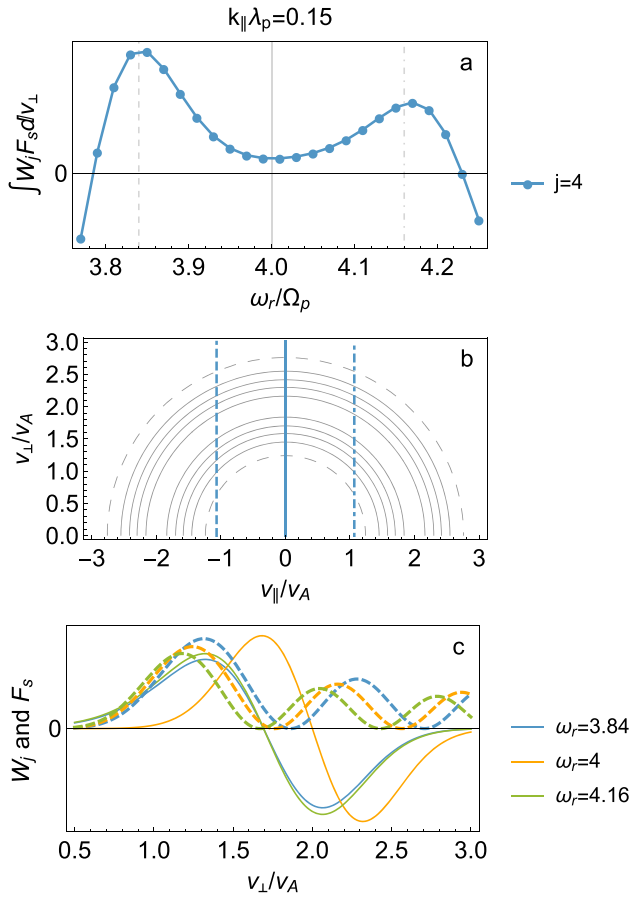

Figure 5. For the case of the shell model and for $k_{\parallel}\lambda_p = 0.15$. (a and c) The figure formats are the same as Figures 3a and 3c. (b) The plot displays contours of the shell distribution function, f_s, and the corresponding parallel resonant speeds. The dashed contours delineate the 10% level of the f_s maximum.

the W_j and F_s terms at the three ω_r values. As with the ring model case, the peak of F_s for $\omega_r/\Omega_p = 4$ is located at the valley of W_j. In contrast to the ring model case, however, the peaks of F_s for $\omega_r/\Omega_p = 3.84$ and 4.16 are located close to the first peaks of W_j due to curved geometry of the shell distribution in gyroaveraged velocity space. So the weighted integrals in equation (16) which is directly proportional to γ are larger at the (slightly) off-harmonic frequencies. As shown in Figure 1c, the two maxima move farther apart from each other as $k_{\parallel}$ increases. This is because in order to keep the more or less same $v_{j,\mathrm{res}}$ values at which γ_{max} tend to occur (see Figure 5b), ω_r has to move farther away from $4\Omega_p$. As a result, it appears as though the two local growth rate maxima split out from a single growth rate peak at $k_{\parallel} \approx 0$ and the exact harmonics of Ω_p as shown in Figure 1c.

Figures 6a and 6b display the same quantities at $k_{\parallel}\lambda_p = 0.5$ and near $\omega_r/\Omega_p = 6$. Unlike the case of the ring model, the terms of $j = 5$ and 7 become important. At $\omega_r/\Omega_p = 6$ (solid vertical line), the resonant speeds are $\pm 2v_A$ for $j = 5$ and 7, respectively, so F_s evaluated at $v_{\parallel} = \pm 2v_A$ is negative for all $v_{\perp}$. It turns out that the damping provided by the cyclotron resonant protons at $v_{\parallel} = \pm 2v_A$ is larger than the growth provided by the cyclotron resonant protons at $v_{\parallel} = 0$ (corresponding to $j = 6$), resulting in the net damping at $\omega_r/\Omega_p = 6$. On the other hand, near the half harmonic at $\omega_r/\Omega_p = 5.5$ (dashed vertical line), the resonant speeds shift altogether toward the left such that $|v_{j,\mathrm{res}}| < v_s$ for $j = 5$ and 6 where F_s can be positive, leading to wave growth near the half harmonic.

Finally, Figures 6c and 6d display the same quantities at $k_{\parallel}\lambda_p = 0.8$ and near $\omega_r/\Omega_p = 6$. Due to the increased $k_{\parallel}$, the interspacing between the neighboring vertical bars in Figure 6d becomes tighter. Consequently, at the exact harmonic of $\omega_r/\Omega_p = 6$ (vertical solid line) $|v_{j,\mathrm{res}}|$ is less than v_s for $j = 5$ and 7, and $v_{j,\mathrm{res}}$s for $j = 4$ and 8 straddle the outskirts of the shell. Since the terms of $j = 5$, 6, and 7 provide growth while the terms of $j = 4$

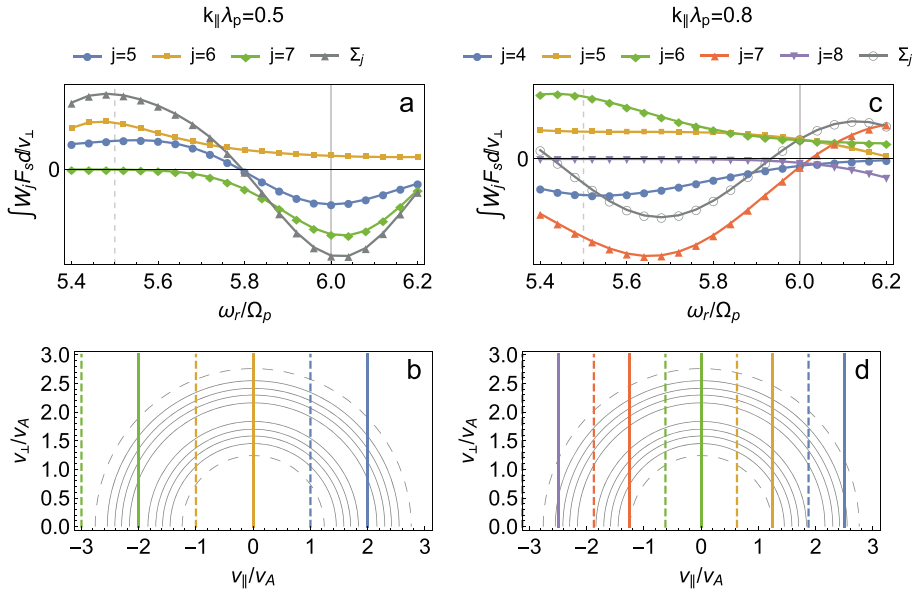

Figure 6. For the case of the shell model and for $k_{\|}\lambda_p$ = (a and b) 0.5 and (c and d) 0.8. The figure format is similar to Figures 4a and 4b, but Figures 4b and 4d display the shell distribution function and the relevant parallel resonant speeds as Figure 3b.

and 8 provide weak damping, the net effect is $\gamma > 0$. On the other hand, near the half harmonic at $\omega_r/\Omega_p = 5.5$ (dashed vertical line), all values of $v_{j,\mathrm{res}}$ again shift to the left such that the protons in the fourth and seventh cyclotron harmonic resonances provide stronger damping (due to $|v_{j,\mathrm{res}}| \approx v_s$) than the growth provided by the protons in the fifth and sixth cyclotron harmonic resonances. In effect, the situation is roughly opposite to the case of $k_{\|}\lambda_p = 0.5$.

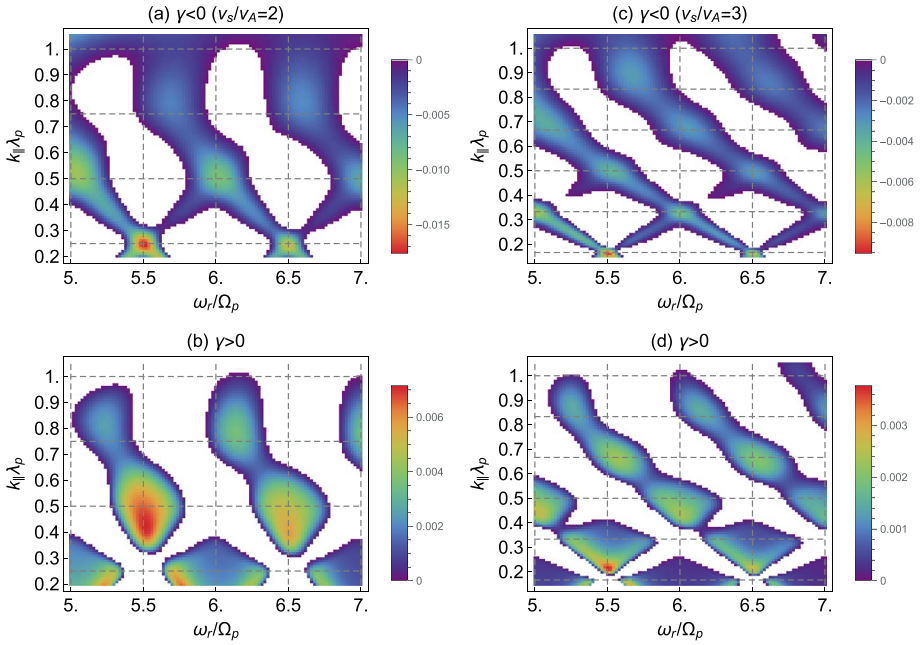

Figure 7. Plots of (top) damping and (bottom) growing modes calculated from the approximate linear theory for the shell models with the shell speed v_s/v_A = (left) 2 and (right) 3 in $k_{\|}$-ω_r space. The horizontal dashed lines are drawn at integral multiples of $\Omega_p/(2v_s)$.

Note that F_s evaluated at $|v_\parallel| \geq v_s$ is always negative. Since more cyclotron resonance terms are involved and the resonant protons at $|v_\parallel| \gtrsim v_s$ predominantly contribute to damping, the overall growth rate decreases rapidly as $k_\parallel$ further increases. Subsequently, compared to the ring model, the instability driven by the shell model is confined to relatively small $k_\parallel$ ($k_\parallel \lambda_p \lesssim 1$), as shown in Figure 1c.

One prominent feature of the growth rate pattern for the shell model shown in Figure 1c is the alternating pattern of growth and damping in frequency and wave number space. Since it is likely that strong damping occurs when $|v_{j,\mathrm{res}}| \approx v_s$ as discussed in the previous paragraphs explaining Figure 6, it may be possible to estimate from the resonance condition that at what $k_\parallel$ exact or half harmonic modes will be stable or unstable. Using the condition $|v_{j,\mathrm{res}}| = v_s$, heavy damping should be expected near the exact harmonics when $k_\parallel = l\Omega_p/v_s$, where $l = 1, 2, 3, \ldots$. Likewise, heavy damping near the half harmonics should be expected when $k_\parallel = (l - 0.5)\Omega_p/v_s$. Therefore, the Bernstein modes should alternate between the damping and growing modes near the full/half harmonics of Ω_p at every $\Delta k_\parallel = \Omega_p/(2v_s)$. To confirm this, Figures 7a and 7b show the damping modes as well as the growing modes calculated using the approximate growth rate formula. For $k_\parallel \lambda_p = 0.25$, damping is strongest at the half harmonics because there are only two relevant cyclotron resonances at $v_\parallel = \pm v_s$. The next strongest damping occurs at the full harmonics for $k_\parallel \lambda_p = 0.5$ where there is an additional cyclotron resonance at $v_{j,\mathrm{res}} = 0$ (solid lines in Figure 6b). Then the next strongest damping appears to occur near $k_\parallel \lambda_p = 0.75$ as expected but somewhat away from the half harmonics. As shown in Figure 6c, the strongest damping for $j = 7$ occurs at $\omega_r/\Omega_p \approx 5.65$. The reason is perhaps that $v_{j,\mathrm{res}}$ becomes less sensitive to ω_r with increasing $k_\parallel$ and the role of W_j becomes important. The next expected heavy damping at the exact harmonics and at $k_\parallel \lambda_p = 1$ is not clear due perhaps to the same reason and the increasing number of cyclotron resonances involved. The pattern of the growing modes is roughly opposite to that of the damping modes, although the strongest growing modes are not so well organized in $k_\parallel$ space as the strongest damping modes are.

From $\Delta k_\parallel = \Omega_p/(2v_s)$, it is clear that the shell speed should be closely related to how quickly growth and damping alternate in $k_\parallel$ space—the larger the shell speed, the denser the alternating pattern should be. Figures 7c and d display the damping and growing modes, respectively, for the shell model with $v_s/v_A = 3$. In this case, the strongest damping modes alternate between full and half harmonics at every $\Delta k_\parallel \lambda_p \approx 1/(2 \cdot 3)$.

5. Summary

In the present study the differences in the linear growth rate patterns of the proton Bernstein instabilities driven by the proton ring and shell velocity distributions have been investigated using approximate linear kinetic theory derived from the extraordinary mode dispersion relation. The results show that the growth rate pattern (particularly where the peaks and valleys occur) is primarily determined by the geometry of the gyroaveraged velocity distribution function and the cyclotron resonance condition, $v_\parallel = (\omega_r - j\Omega_p)/k_\parallel$.

For proton velocity distributions involving a ring distribution, the unstable modes are discrete in frequency space at small $k_\parallel$. They approximately follow the exact proton cyclotron harmonic frequencies and broaden in frequency space as $k_\parallel$ gradually increases. These discrete modes eventually merge into a continuum when $k_\parallel$ is sufficiently large. All these features are related to the fact that the resonant speeds are very sensitive to changes in ω_r at small $k_\parallel$ but become less sensitive as $k_\parallel$ increases and that the ring speed is independent of the parallel velocity component. As a result, the parallel thermal spread of the ring distribution should be closely related to the minimum $k_\parallel$ at which the continuum starts to appear: the larger the thermal speed, the smaller this minimum.

On the other hand, for proton velocity distributions involving a shell distribution (f_s), the curved geometry of the shell distribution in gyroaveraged velocity space results in a complex alternating pattern of growth and damping rates in frequency and wave number space, and confines the unstable Bernstein modes to relatively small $k_\parallel$. When $k_\parallel$ increases, the unstable modes do not follow the proton cyclotron harmonic frequencies but split into two local peaks on both sides of the corresponding harmonic frequencies. Strong damping of the instabilities occurs when the protons with $|v_\parallel| = v_s$ satisfy the resonance condition, because these protons have overall the most negative $\partial f_s/\partial v_\perp$. Subsequently, the shell speed closely controls the density of this alternating pattern ($\Delta k_\parallel = \Omega_p/(2v_s)$). In addition, the thermal spread of the shell should not significantly change the pattern itself but affects its sharpness: the larger the thermal spread, the fuzzier the pattern.

Acknowledgments
Data supporting the figures presented are available upon request from the corresponding author. The work at Auburn University was supported by NSF grant 1303623. Authors thank S. Peter Gary for helpful discussion.

References

Balikhin, M. A., Y. Y. Shprits, S. N. Walker, L. Chen, N. Cornilleau-Wehrlin, I. Dandouras, O. Santolík, C. Carr, K. H. Yearby, and B. Weiss (2015), Observations of discrete harmonics emerging from equatorial noise, *Nat. Commun.*, *6*, 7703, doi:10.1038/ncomms8703.

Boardsen, S. A., D. L. Gallagher, D. A. Gurnett, W. K. Peterson, and J. L. Green (1992), Funnel-shaped, low-frequency equatorial waves, *J. Geophys. Res.*, *97*(A10), 14,967–14,976, doi:10.1029/92JA00827.

Chen, L. (2015), Wave normal angle and frequency characteristics of magnetosonic wave linear instability, *Geophys. Res. Lett.*, *42*, 4709–4715, doi:10.1002/2015GL064237.

Chen, L., R. M. Thorne, V. K. Jordanova, C.-P. Wang, M. Gkioulidou, L. Lyons, and R. B. Horne (2010a), Global simulation of EMIC wave excitation during the 21 April 2001 storm from coupled RCM-RAM-HOTRAY modeling, *J. Geophys. Res.*, *115*, A07209, doi:10.1029/2009JA015075.

Chen, L., R. M. Thorne, V. K. Jordanova, and R. B. Horne (2010b), Global simulation of magnetosonic wave instability in the storm time magnetosphere, *J. Geophys. Res.*, *115*, A11222, doi:10.1029/2010JA015707.

Chen, L., R. M. Thorne, V. K. Jordanova, M. F. Thomsen, and R. B. Horne (2011), Magnetosonic wave instability analysis for proton ring distributions observed by the LANL magnetospheric plasma analyzer, *J. Geophys. Res.*, *116*, A03223, doi:10.1029/2010JA016068.

Chen, L., R. M. Thorne, Y. Shprits, and B. Ni (2013), An improved dispersion relation for parallel propagating electromagnetic waves in warm plasmas: Application to electron scattering, *J. Geophys. Res. Space Physics*, *118*, 2185–2195, doi:10.1002/jgra.50260.

Chen, L., J. Sun, Q. Lu, X. Gao, Z. Xia, and Z. Zhima (2016), Generation of magnetosonic waves over a continuous spectrum, *J. Geophys. Res. Space Physics*, *121*, 1137–1147, doi:10.1002/2015JA022089.

Dendy, R. O., and K. G. McClements (1993), Ion cyclotron wave emission at the quasi-perpendicular bow shock, *J. Geophys. Res.*, *98*(A9), 15,531–15,539, doi:10.1029/93JA01386.

Denton, R. E., M. J. Engebretson, A. Keiling, A. P. Walsh, S. P. Gary, P. M. E. DéCréAu, C. A. Cattell, and H. RèMe (2010), Multiple harmonic ULF waves in the plasma sheet boundary layer: Instability analysis, *J. Geophys. Res.*, *115*, A12224, doi:10.1029/2010JA015928.

Gary, S. P., K. Liu, D. Winske, and R. E. Denton (2010), Ion Bernstein instability in the terrestrial magnetosphere: Linear dispersion theory, *J. Geophys. Res.*, *115*, A12209, doi:10.1029/2010JA015965.

Gary, S. P., K. Liu, and D. Winske (2011), Bernstein instability driven by suprathermal protons in the ring current, *J. Geophys. Res.*, *116*, A08215, doi:10.1029/2011JA016543.

Gul'elmi, A., B. Klaine, and A. Potapov (1975), Excitation of magnetosonic waves with discrete spectrum in the equatorial vicinity of the plasmapause, *Planet. Space Sci.*, *23*(2), 279–286, doi:10.1016/0032-0633(75)90133-6.

Gurnett, D. A. (1976), Plasma wave interactions with energetic ions near the magnetic equator, *J. Geophys. Res.*, *81*(16), 2765–2770, doi:10.1029/JA081i016p02765.

Horne, R. B., G. V. Wheeler, and H. S. C. K. Alleyne (2000), Proton and electron heating by radially propagating fast magnetosonic waves, *J. Geophys. Res.*, *105*(A12), 27,597–27,610, doi:10.1029/2000JA000018.

Hrbáčková, Z., O. Santolík, F. Němec, E. Macúšová, and N. Cornilleau-Wehrlin (2015), Systematic analysis of occurrence of equatorial noise emissions using 10 years of dathe Cluster mission, *J. Geophys. Res. Space Physics*, *120*, 1007–1021, doi:10.1002/2014JA020268.

Kennel, C. (1966), Low-frequency whistler mode, *Phys. Fluids*, *9*(11), 2190–2202, doi:10.1063/1.1761588.

Liu, K., S. P. Gary, and D. Winske (2011), Excitation of magnetosonic waves in the terrestrial magnetosphere: Particle-in-cell simulations, *J. Geophys. Res.*, *116*, A07212, doi:10.1029/2010JA016372.

Ma, Q., W. Li, R. M. Thorne, and V. Angelopoulos (2013), Global distribution of equatorial magnetosonic waves observed by THEMIS, *Geophys. Res. Lett.*, *40*, 1895–1901, doi:10.1002/grl.50434.

Ma, Q., W. Li, L. Chen, R. M. Thorne, and V. Angelopoulos (2014), Magnetosonic wave excitation by ion ring distributions in the Earth's inner magnetosphere, *J. Geophys. Res. Space Physics*, *119*, 844–852, doi:10.1002/2013JA019591.

Ma, Q., W. Li, R. M. Thorne, J. Bortnik, C. A. Kletzing, W. S. Kurth, and G. B. Hospodarsky (2015), Electron scattering by magnetosonic waves in the inner magnetosphere, *J. Geophys. Res. Space Physics*, *121*, 274–285, doi:10.1002/2015JA021992.

McClements, K. G., R. O. Dendy, and C. N. Lashmore-Davies (1994), A model for the generation of obliquely propagating ULF waves near the magnetic equator, *J. Geophys. Res.*, *99*(A12), 23,685–23,693, doi:10.1029/94JA01979.

Meredith, N. P., R. B. Horne, and R. R. Anderson (2008), Survey of magnetosonic waves and proton ring distributions in the Earth's inner magnetosphere, *J. Geophys. Res.*, *113*, A06213, doi:10.1029/2007JA012975.

Min, K., and K. Liu (2015a), Fast magnetosonic waves driven by shell velocity distributions, *J. Geophys. Res. Space Physics*, *120*, 2739–2753, doi:10.1002/2015JA021041.

Min, K., and K. Liu (2015b), Regime transition of ion Bernstein instability driven by ion shell velocity distributions, *J. Geophys. Res. Space Physics*, *120*, 8448–8454, doi:10.1002/2015JA021514.

Min, K., and K. Liu (2016), Proton velocity ring-driven instabilities in the inner magnetosphere: Linear theory and particle-in-cell simulations, *J. Geophys. Res. Space Physics*, *121*, 475–491, doi:10.1002/2015JA022042.

Min, K., K. Liu, and S. P. Gary (2016), Scalings of Alfvén-cyclotron and ion Bernstein instabilities on temperature anisotropy of a ring-like velocity distribution in the inner magnetosphere, *J. Geophys. Res. Space Physics*, *121*, doi:10.1002/2015JA022134.

Němec, F., O. Santolík, K. Gereová, E. Macúšová, Y. de Conchy, and N. Cornilleau-Wehrlin (2005), Initial results of a survey of equatorial noise emissions observed by the Cluster spacecraft, *Planet. Space Sci.*, *53*(1–3), 291–298, doi:10.1016/j.pss.2004.09.055.

Němec, F., O. Santolík, K. Gereová, E. Macúšová, H. Laakso, Y. de Conchy, M. Maksimovic, and N. Cornilleau-Wehrlin (2006), Equatorial noise: Statistical study of its localization and the derived number density, *Adv. Space Res.*, *37*(3), 610–616, doi:10.1016/j.asr.2005.03.025.

Perraut, S., A. Roux, P. Robert, R. Gendrin, J.-A. Sauvaud, J.-M. Bosqued, G. Kremser, and A. Korth (1982), A systematic study of ULF waves above f_{H+} from GEOS 1 and 2 measurements and their relationships with proton ring distributions, *J. Geophys. Res.*, *87*(A8), 6219–6236, doi:10.1029/JA087iA08p06219.

Posch, J. L., M. J. Engebretson, C. N. Olson, S. A. Thaller, A. W. Breneman, J. R. Wygant, S. A. Boardsen, C. A. Kletzing, C. W. Smith, and G. D. Reeves (2015), Low-harmonic magnetosonic waves observed by the Van Allen Probes, *J. Geophys. Res. Space Physics*, *120*, 6230–6257, doi:10.1002/2015JA021179.

Press, W. H., B. P. Flannery, S. A. Teukolsky, and W. T. Vetterling (1992), *Numerical Recipes*, Cambridge Univ. Press, New York.

Russell, C. T., R. E. Holzer, and E. J. Smith (1970), OGO 3 observations of ELF noise in the magnetosphere: 2. The nature of the equatorial noise, *J. Geophys. Res.*, *75*(4), 755–768, doi:10.1029/JA075i004p00755.

Santolík, O., F. Němec, K. Gereová, E. Macúšová, Y. de Conchy, and N. Cornilleau-Wehrlin (2004), Systematic analysis of equatorial noise below the lower hybrid frequency, *Ann. Geophys.*, *22*(7), 2587–2595, doi:10.5194/angeo-22-2587-2004.

Stix, T. H. (1992), *Waves in Plasmas*, Am. Inst. of Phys., New York.

Thomsen, M. F., M. H. Denton, V. K. Jordanova, L. Chen, and R. M. Thorne (2011), Free energy to drive equatorial magnetosonic wave instability at geosynchronous orbit, *J. Geophys. Res.*, *116*, A08220, doi:10.1029/2011JA016644.

Umeda, T., S. Matsukiyo, T. Amano, and Y. Miyoshi (2012), A numerical electromagnetic linear dispersion relation for Maxwellian ring-beam velocity distributions, *Phys. Plasmas*, *19*(7), 072107, doi:10.1063/1.4736848.

Vandas, M., and P. Hellinger (2015), Linear dispersion properties of ring velocity distribution functions, *Phys. Plasmas*, *22*(6), 062107, doi:10.1063/1.4922073.

Walker, S. N., M. A. Balikhin, D. R. Shklyar, K. H. Yearby, P. Canu, C. M. Carr, and I. Dandouras (2015), Experimental determination of the dispersion relation of magnetosonic waves, *J. Geophys. Res. Space Physics*, *120*, 9632–9650, doi:10.1002/2015JA021746.

Xiao, F., Q. Zhou, Z. He, C. Yang, Y. He, and L. Tang (2013), Magnetosonic wave instability by proton ring distributions: Simultaneous data and modeling, *J. Geophys. Res. Space Physics*, *118*, 4053–4058, doi:10.1002/jgra.50401.

Zhou, Q., et al. (2014), Excitation of nightside magnetosonic waves observed by Van Allen Probes, *J. Geophys. Res. Space Physics*, *119*, 9125–9133, doi:10.1002/2014JA020481.